Grain alignment and its relationship with superconductivity and thermal transport of Ni-substituted Bi-2212 textured rods fabricated at two different growth rates

M. Ozabaci[a,*], O. Kizilaslan[b], M.A. Madre[c], M.E. Yakinci[a,d] and A. Sotelo[c]

[a] *Scientific and Technological Research Center, Inonu University, 44280-Malatya, Turkey*
[b] *Department of Physics,Faculty of Arts and Sciences, Inonu University,44280-Malatya,Turkey*
[c] *ICMA (CSIC- Universidad de Zaragoza) C/Maria de Luna, 3, 50018-Zaragoza, Spain*
[d] *Department of Biomedical Engineering, Faculty of Engineering, Inonu University, 44280-Malatya, Turkey*

Abstract

The microstructure, grain alignment, superconducting and thermal transport properties of Ni-substituted Bi-2212 rods grown at two different speeds (15 and 30 mm/h) through the Laser Floating Zone (LFZ) method, have been evaluated. Significant variations in grain size, grain alignment, electrical and thermoelectric power properties have been observed for the rods depending on the growth and substitution rates. The highest aligned structure was obtained on unsubstituted rods grown at 15 mm/h. Both increased substitution and growth rates degraded the grain alignment. The presence of Ni-based secondary phases showed that Ni is not totally incorporated into the crystal structure, which, in turn, caused a decrease on the average grain size of the rods. With increasing Ni concentration, peak values of thermoelectric power of the rods, which lie between 3.8 and 6.4 μVK^{-1}, monotonically decreased while thermal conductivity values did not show any systematic change. The activation energy of flux motion, U_o, was calculated from the field dependent resistivity–temperature curves in a range of 0-8 T. Superconducting transition temperatures, T_c^{onset} and T_c^{offset}, and activation energy, U_o, were found to decrease with increasing Ni contents and applied magnetic field. It has been estimated from the magnetic field dependence of activation energy of the samples that plastic creep of the collective vortices is dominant in the rods.

Keywords: High-T_c superconductors, Laser processing, Aligned Structure, Pole Figure, Thermal Transport, Activation Energy.

*Corresponding author. Tel.:+90 4223774956
E-mail address: muratozabaci@yahoo.com (M.Ozabaci)

1. Introduction

The main obstacles for the technological applications of high temperature superconductors (HTSs) are caused by weak connectivity of grains and high anisotropy of physical properties [1-4]. Melt texturing is one of the important tools to overcome these type of limitations by reducing the number of grain boundaries and increasing the preferred orientation of grains on the whole bulk [5-7]. Laser Floating Zone (LFZ) method has proved its capability in fabricating highly oriented Bi-2212 rod shaped crystals as well as films and single crystals [8-11].

The rods obtained by this route have important technological applications as current leads and fault current limiters [12-14]. HTS current leads are often used in transmitting large currents from room-temperature power supplies to very low-temperature superconducting coils [15]. Because of low thermal conductivity and high current carrying capacity of HTSs, significant amount of cooling cost saving becomes probable with use of the HTS current leads [16,17].

Because of the crucial importance of the current carrying capacity of the materials used as current leads, the researches on LFZ Bi-2212 rods have mainly focused on developing high critical current density properties. Most of these studies include adjustment of LFZ processing conditions as well as stoichiometric modifications of precursor powders [18-22]. Substitution of foreign elements into the Bi-2212 structure has created different effects on superconducting and mechanical properties of the LFZ rods. It has been shown that adding of Ag up to 1 wt.% improved the microstructure and mechanical strength by reducing the porosity [23, 24]. Similarly, MgO addition to Bi-2212 flat monoliths realized by a different laser processing method (laser zone melting, LZM) strengthen the critical current density by a factor of 3 without any observable degradation on texturing level [25]. In contrast, addition of 2 at.% Ti degraded both texturing and superconducting parameters of rods by introducing bubbles into the structure which eventually causes a decrease in grain size [26].

It is widely accepted that very effective tools for investigation of the current carrying properties of superconductors are the determination of the grain alignment level and activation energy of flux motion, which is a measure of the flux pinning ability of the superconductor. In this study, pole figure measurements and field-dependent resistivity temperature curves are used to estimate these two parameters.

The work reported here aims to reveal the relationship between grain alignment, superconducting and thermal transport properties of textured Bi-2212 superconducting rods grown at two different rates, together with Ni substitution for Cu as described by the general formula $Bi_2Sr_2Ca_1Cu_{2-x}Ni_xO_{8+\delta}$ where x = 0, 0.01, 0.03, 0.05 and 0.1.

2. Experimental

$Bi_2Sr_2Ca_1Cu_{2-x}Ni_xO_{8+\delta}$ (x=0, 0.01, 0.03, 0.05 and 0.1) powders were prepared by the classical solid state route from commercially available Bi_2O_3 (Panreac, 98+%), $SrCO_3$ (Panreac, 98+%), $CaCO_3$ (Panreac, 98.5+%), CuO (Panreac, 97+%) and NiO (Aldrich, 99%) powders. The weighed powders were ball-milled using agate balls and acetone media for 30 minutes at 300 rpm to obtain a homogeneous mixture. The obtained suspension was dried using IR radiation in order to evaporate the acetone. The resulting mixture was placed in a furnace and heated to 750 ^{o}C, kept for 12 h, and then slowly cooled down to room temperature. After cooling, the powder was ground and re-heated at 800 ^{o}C for 12 h, milled and isostatically pressed at approximately 200 MPa in form of cylinders (1.5–3 mm diameter and 120 mm long).

The obtained cylinders were subsequently used both as feed and seed in LFZ process as described elsewhere [27]. The textured bars were obtained using a continuous power Nd:YAG laser (λ=1064 nm), under air, at growth rates of 15 and 30 mm h^{-1} and a relative rotation of 18 rpm between seed (3 rpm, clockwise) and feed (15 rpm, anticlockwise). The growth speeds applied in this study correspond to downwards movement of seed at speeds of 15 and 30 mm h^{-1} while the feed has been moved at 12 and 24 mm h^{-1}, respectively. For each growth rate 5 rods of each composition were fabricated. From now on, the rods will be called G15 and G30 for growth rates of 15 and 30 mm h^{-1}, respectively. As Bi-2212 compounds melt incongruently, after laser processing, the rods need a final thermal treatment to reach pure Bi-2212 superconducting phase. This annealing process consisted of two steps: 60 h at 860 ^{o}C, followed by 12 h at 800 ^{o}C and, finally, quenched in air to room temperature. These bars were finally cut to obtain samples having the adequate dimensions for their characterization.

In order to evaluate the grain orientation in the rods pole figures centered in the (020) plane of the Bi-2212 phase, acquired on polished transversal cross sections, were measured by the

Schulz reflection method with Cu Kα radiation. The tilt angle (α) was varied from 15 to 90^{o} while the angle of rotation, azimuth angle (β), was varied from 0 to 360^{o}. For the pole figure measurements Rigaku Rint 2000 powder diffractometer was used.

Phase analysis of all samples was performed by powder XRD utilizing a Rigaku RadB X-ray powder diffractometer (Cu Kα radiation) with 2θ ranging between 5 and 65 degrees. Microstructural and elemental analysis of the fibers, both as-grown and annealed, were studied on polished longitudinal cross-sections by using LEO EVO-40 XVP scanning electron microscope (SEM) equipped with a Bruker energy dispersive X-ray spectroscope (EDX).

Electrical measurements were performed with Quantum Design PPMS (9 T) system. Superconducting transition temperature was determined from resistivity measurements of the samples against temperature. Electrical resistivity of the samples was measured between 5 K and 300 K using the conventional four-probe configuration. 1 mA AC (17 Hz) current was applied during *R*-*T* measurements. Magnetoresistivity measurements were made also for the all samples under DC magnetic fields of 0, 2, 4, 6 and 8 T with the applied magnetic field perpendicular to the current flow direction.

Thermal conductivity and thermopower (Seebeck coeffiecient) measurements were also realized in Quantum Design PPMS operating in thermal transport option on 1 cm long samples. The two-probe lead configuration method was used for the measurements, which is the most convenient because it involves attaching only two leads. In this configuration, heater/I+ and T_{hot}/V+ share one lead while coldfoot/I− and T_{cold}/V−share the other lead. These shoes monitor both the temperature and voltage drops simultaneously across the sample after applied low-frequency, square-wave heat pulse from heater in the temperature range of 15-275 K. The thermal conductivity, κ, is then derived by the expression, $\kappa=KL/A$, where L and A are the length and the cross-sectional area of the sample, respectively. The equation used to calculate Seebeck coefficient is $\alpha=\Delta V/\Delta T$.

3. Results and discussion

3.1. XRD and pole figure analyses

Powder X-ray diffraction patterns and corresponding (*hkl*) Miller indices of the G30 rods after final thermal treatment are shown in Figure 1a-e, as representative of all the samples. All the main XRD peaks of the pure and slightly substituted samples were identified and

indexed for the Bi-2212 phase with no secondary ones. For the highest substituted sample (Figure 1e), a small peak at $2\theta=29.9^{o}$ belonging to low-T_c phase (Bi-2201) was identified which indicates that high amount of Ni promotes the decomposition of the Bi-2212 phase.

Figure 2a-d shows the pole figures of the slightly and highly doped (x=0.03 and x=0.1, respectively) rods processed at two different growth speeds as representative examples. Color scales and α dependence of average intensity of reflected X-rays of associated samples are also seen next to pole figures. It has been found that increasing α values lead to higher counts for the all rods which seems as a strong evidence of the aligned structure of the rods. In order to compare the alignment degree of the rods, numeric values were obtained by dividing the counts at $\alpha=90^{o}$ to the counts at $\alpha=60^{o}$ for the each rod. These values, displayed in Table I, showed that G15 rods possess stronger orientation than the obtained in the G30 ones. On the other hand, Ni substitution differently affects the rods grown at different speeds. For the G30 rods, increased substitution rate did not give rise to any significant difference on the alignment degree of the rods. On the other hand, the alignment of G15 rods followed a different route depending on the substitution level: while alignment degree of the rods remains at almost same level for the $x\leq0.03$ range, after this amount, Ni substitution strongly degraded the alignment of the G15 rods. It was seen that, at the highest substitution used, the alignment of the G15 rods approached to G30 ones.

3.2. SEM/EDX observations

There are two main phases appearing on polished longitudinal cross-section of as-grown rods in SEM/EDX investigations, as can be observed in Fig.3a-d. These are Bi-rich intergrowths of 2201 and 2212 as a main matrix and Bi-free $Sr_{1-x}Ca_xCuO_2$ phase which can be seen as gray and black contrasts, respectively, on the BSD images of the rods. The most important effect caused by Ni substitution on the morphology of the rods is the fact that the size of the grains decreases when the Ni content is increased (Fig 3a-b). Moreover, at low doping, the amount of secondary phases is slightly higher on as-grown G30 rods than that of G15 ones. Upon annealing, although minor amounts of metallic oxides persist especially at the edges of the rods (Fig.3c), Bi-2212 phase is formed and covers all the volume following the reaction of above mentioned two phases. Elemental mapping image in Figure 3d shows that most of the substituted Ni atoms are randomly distributed all along the volume of the

rods while tiny part of them gives rise to a new Sr-Ni-rich Bi-2212 phase which appears as darker grey contrast with elongated shape, on the BSD images for doping levels x≥0.5.

3.3. Electrical resistivity properties

The normalized electrical resistivity versus temperature curves for all the samples are given in Fig. 4. All the samples show metallic behavior above T_c^{onset} values and below this value zero-resistance state appears within a narrow temperature range. Increased substitution rate produces a downward shift on both of the superconducting transition temperatures, T_c^{onset} and T_c^{offset}. At the same time, a broadening on the transition was obtained in the resistivity curves when the doping level is increased. These effects can be associated with the effect of Ni on the Bi-2212 phase which eventually leads to changes on the hole carrier concentration from the optimal values. The magnetic moments introduced by Ni impurities might also create these effects by increasing the sensitivity of the superconducting carriers to the grain boundaries.

For the undoped samples, T_c^{onset} , T_c^{offset} and ΔT values of G15 and G30 rods were obtained to be 96 K, 89 K, 7 K and 96.5 K, 89.5 K, 7 K, respectively. When the substitution is increased to x=0.1, T_c^{onset} and T_c^{offset} values of the both G15 and G30 samples decreased to the same values: 88 K and 77.5 K, respectively, while ΔT of the rods is raised to 10.5 K. This suggests that the different growth rates applied in this study do not affect the electrical properties of the rods in a significant manner which can be related to similar phase distribution in the G15 and G30 rods after the final thermal treatment. At the same time, it is seen that critical temperatures of the rods are not directly connected with the alignment degree of the structures, as expected. Room temperature resistivity values of the rods (ρ_{rt}) have been found to be in the range of 9-23 mΩ.cm, irrespective of applied substitution and growth rates.

3.4. Magnetoresistivity properties

Fig. 5 shows the magnetoresistance measurements of the pure and the highest-substituted G15 and G30 rods. It is clear from Fig. 5 that increasing magnetic field, up to 8 T, weakly affect the onset of superconductivity. On the other hand, T_c^{offset} values showed a strong decrease depending on increasing magnetic field. For example, the magnitude of decrease of

T_c^{onset} values of x=0.1, G15 and G30 rods, under applied magnetic field of 8 T, is limited to 3 K (from 88 K to 86 K) while that of T_c^{offset} values is around 36.5 K (from 77.5 K to around 41 K). This type of behavior is often observed on cuprates having high crystal quality and compact structures. Another effect of increasing the magnetic field is the appearance of resistive tails on the lower temperature end of *R-T* curves which is related with energy dissipation mechanism stemming from motion of fluxons under the influence of the Lorentz force and thermal energy. These effects increase with increasing magnetic field. Regarding the decrement of critical temperature values and the shape of *MR-T* curves, it seemed that increased magnetic field almost equally affected the rods grown at two different speeds with various substitution rates.

3.4.1. Calculations of activation energy

The thermal energy causing motion of vortices and, eventually, the dissipation of energy, as mentioned above, is known as thermally activated flux flow (TAFF). The broadening of the resistive transition in the presence of magnetic field near T_c is attributed to the TAFF [28-30]. Therefore, resistance caused by TAFF is described by the well-known Arrhenius equation, $\rho\,(B,T) = \rho_0 \exp(-U_o/k_B T)$, where ρ_0 is the pre-exponential factor, k_B is Boltzmann's constant and U_0 is the activation energy which is necessary for the motion of vortices out of the pinning potential wells and gives the magnitude of the effective pinning energy.

Fig. 6 shows Arrhenius plot of resistivity of the x=0 and 0.1 substituted G15 and G30 samples. In this figure, the activation energies, depending on both substitution and growth rates, are extracted from the slope of linear part of the low resistivity region, one of which is shown in Fig. 6a as an example, and given in Fig. 7. Since the difference in the activation energies of the unsubstituted and slightly substituted (x=0.01, 0.03 and 0.05) samples is very low, x=0 and x=0.1 samples are selected as representatives of the series.

It is clearly seen in the figures that both increased substitution and growth rates as well as increased magnetic field degrade the activation energies of the samples. At zero applied field, the activation energy of the samples take values from 0.64 eV for the x=0.1-G30 rods to 0.81 eV for the x=0-G15 ones and they decrease to 0.032 and 0.047 eV under 8 T, respectively. These values are in the same order of magnitude of the previously reported for Bi-2212 crystals [31,32].

The slope of the double logarithmic scale of $U_0 - H$ (Fig. 7) gives information about magnetic field dependence of the activation energy and hence it provides unique chance to understand the physical phenomena behind of the vortex motion. In the figure, a decrease of activation energy with magnetic field was clearly observed. The decrease of activation energy exhibited a power-law field dependence, $U_0 \sim H^{-n}$, which is generally observed on layered structures [33-35]. The experimental results were fitted to this equation and the fitting parameter, n, was found to be 0.40, 0.45, 0.37 and 0.44 for x=0-G15, x=0-G30, x=0.1-G15 and x=0.1-G30 rods, respectively.

The magnitude of the n value determines the type of vortex creep motion. If the plastic creep is dominant, n value should be 0.5 [36-38]. The n values obtained in this study, which are close to 0.5, suggest that plastic creep of the collective vortices is dominant in the rods.

3.5. Thermal conductivity properties

The variation of the thermal conductivity with temperature, *κ(T)*, for the G15 and G30 rods substituted at the rates of x=0, 0.01, 0.05 and 0.1 are shown in Fig 8a-b. Since the thermal conductivity measurements were realized along the rod axis, as explained in section 2, the major contribution to the measured *κ(T)* comes from the in-plane component $\kappa_{ab}(T)$. In the normal state, the conductivities of all the samples follow parallel trends. *κ* decreased linearly as temperature decreases to around T_c^{onset} which is a characteristic feature of high temperature superconducting materials [39-42]. Since most of the heat is carried by phonons in the normal state, the linear decrease of κ above T_c^{onset} is associated with the weakening of the phonon scattering contribution to the total heat transport from point defects, phonons, dislocations and electrons. This decrease is followed by a small minimum around 120 K, then an upturn, with a broad maximum at around 70 K, which is more apparent for slightly substituted rods, and a sharp decrease below. Even if the dominating thermal transport mechanism is not known, the broad maximum appearing has been associated with the extended mean free path of either phonons or quasiparticles due to the reduction of resistive interactions among heat carriers after condensation of electrons into Cooper pairs [43-46].

The peak under T_c is suppressed then disappears upon increased substitution rate. Since the appearance of this peak is believed to depend on the crystal quality of the sample [47], this

behavior points out that increased substitution rates intensify crystal imperfections. This result is partly in accordance with the pole figure and SEM measurements which show a decrement in the grain alignment and grain size of G15 rods at high substitution rates. The magnitude of thermal conductivity, at 150 K, lies between 0.9-1.5 $Wm^{-1}K^{-1}$ and 1-1.7 $Wm^{-1}K^{-1}$ for G15 and G30 rods, disregarding applied substitution rates that could not be sufficient to create crucial changes on interactions of heat carriers. The obtained values are comparable to those of other different shaped Bi-based cuprates and reach as high as 4 $Wm^{-1}K^{-1}$ in single crystals of BSCCO far from crystal defects [47-50].

3.6. Thermoelectric power properties

The temperature dependence of the thermoelectric power or Seebeck coefficient, S, for the x=0, 0.01, 0.05 and 0.1 substituted rods is depicted in Fig 8c-d. The positive sign of thermoelectric power (TEP) values of all the samples over the entire temperature range indicates an electrical conduction mainly governed by holes [51]. With decreasing temperature, TEP increased linearly and attained a maximum value just above T_c^{onset} and then dropped abruptly to zero following the disappearance of voltage on the samples originated by superconducting fluctuations [52]. Such behavior of the TEP has been inferred earlier from similar studies on cuprates and has been analyzed in terms of some phenomenological theoretical models as the Hubbard [53], Two-Band [54] and Nagaosa-Lee [55] model to describe the basic physics of these materials. But this kind of analysis is considered to be the subject of another study.

In the present study, it is clearly observed in the figure that increased Ni content decreased the TEP values of the samples in a wide temperature range. The TEP peak values decreased from 5.5 (G15) and 6.4 μVK^{-1} (G30) belonging to the unsubstituted samples (x=0) to 3.8 (G15) and 5.1 μVK^{-1} (G30) for the highest substituted samples (x=0.1). As can be easily observed, G15 rods possess lower TEP values than G30 ones due to their lower electrical resistivity. which is attributed to the decrease of hole carrier concentration after increased Ni substitution as obtained in *R-T* measurements. On the other hand, it is observed that TEP values of the rods are not directly proportional with their alignment level. The higher aligned structures of G15 rods produced lower TEP values than G30 rods. The physical phenomena

explaining this relationship needs to be further studied regarding different theoretical approaches.

4. Conclusions

The variations of microstructure, alignment level, electrical, pinning potential and thermal transport properties (thermal conductivity and thermoelectric power) of LFZ-grown Bi-2212 rods induced by Ni-substitution and different growing rates have been studied.

It has been found that the highest Ni substitution has partly caused the decomposition of Bi-2212 into the low-T_c superconducting Bi-2201 phase. The decrease of critical temperature values of the samples when Ni substitution is raised was attributed to the decrease of hole carrier concentration due to the decomposition of Bi-2212 phase. The decrease of resistivity from the G30 to the G15 samples has led to lower TEP values. On the contrary, it was obtained that the magnitude of the thermal conductivity of the samples is not very sensitive to the changes, at least at this level, occurred on phase distribution, grain size and alignment.

Pole figure studies indicated that LFZ technique produces better alignment on Bi-2212 rods when growth at 15 mm/h than at 30 mm/h. Alignment level of G15 rods was strongly degraded by Ni substitution whereas G30 ones remained almost unchanged. EDX mapping images showed that Ni is randomly distributed in the structure. It is believed that the decrease of grain size and alignment of the samples with increasing Ni substitution is strictly related with the modification of the solidification mechanism.

The TAFF activation energy or pinning potential of the rods was also calculated using Arrhenius equation. These calculations showed that these values, which are strongly related with current carrying capacity of the rods under magnetic field, are depressed by increasing Ni substitution and growth rates.

Acknowledgements

This work was supported by the Scientific and Technological Research Council of Turkey (TUBITAK) under 2214 International Doctoral Research Fellowship Program. A. Sotelo and M.A. Madre acknowledge DGA (Consolidated research group T12) for financial support. M. A. Madre acknowledges MINECO-FEDER (Project MAT2011-22719) for funding.

References

[1] Y.H. Shi, J.H. Durrell, A.R. Dennis, N. Hari Babu, C.E. Mancini, D.A. Cardwell, Supercond. Sci. Technol. 25 (2012) 045006.
[2] J.R. Kirtley, Rep. Prog. Phys.73 (2010) 126501.
[3] T. Shen, J. Jiang, F. Kametani, U.P. Trociewitz, D.C. Larbalestier, J. Schwartz, E.E. Hellstrom, Supercond. Sci. Technol. 23 (2010) 025009.
[4] S. Vinu, P.M. Sarun, R. Shabna, U. Syamaprasad, J. Appl. Phys. 106 (2009) 063920.
[5] D.F. Zhou, M. Izumi, M. Miki, B. Felder,T. Ida, M. Kitano, Supercond. Sci. Technol. 25 (2012) 103001.
[6] P.V. Parimi, S.B. Vummethala, IEEE T. Appl. Supercon. 9 (1999) 4624-4627.
[7] T.D. Aksenova, P.V. Bratukhin, S.V. Shavkin, V.L. Melnikov, E.V. Antipova, N.E. Khlebova, A.K. Shikov, Physica C, 205 (1993) 271-279.
[8] M. Mora, V. Lennikov, H. Amaveda, L.A. Angurel, G.F. de la Fuente, M.T. Bona, C. Mayoral, J.M. Andres, J. Sanchez-Herencia, IEEE T. Appl. Supercon. 19 (2009) 3041-3044.
[9] M.F. Carrasco, V.S. Amaral, R.F. Silva, F.M. Costa, Appl. Surf. Sci. 257 (2011) 5283–5286.
[10] M. Mora, F. Gimeno, L.A. Angurel, G.F. de la Fuente, Supercond. Sci. Technol. 17 (2004) 1133–1138.
[11] M.R.B. Andreeta, E.R.M. Andreeta, A.C. Hernandes, R.S. Feigelson, J. Cryst. Growth 234 (2002) 759–761.
[12] L. Garcia-Tabares, J. Calero, P. Abramian, F. Toral, L.A. Angurel, J.C. Diez, R. Burriel, E. Natividad, R. Iturbe, J. Etxeandia, IEEE T. Appl. Supercon. 11 (2001) 2543-2546.
[13] F. Lera ,L.A. Angurel, J.A. Rojo ,M. Mora, S. Recuero, M.P. Arroyo, N. Andres, Supercond. Sci. Technol. 18 (2005) 1489–1495.
[14] L.A. Angurel, J.C. Díez, G.F. de la Fuente, F. Gimeno, F. Lera, C. López-Gascón, E. Martínez, M. Mora, R. Navarro, A. Sotelo, N. Andrés, S. Recuero, M. P. Arroyo, phys. stat. sol. (a) 203 (2006) 2931–2937.
[15] R. Wesche, P. Bruzzone, S. March, M. Vogel, H. Ehmler, P. Smeibidl, Phys. Procedia 36 (2012) 927–930.
[16] A. Ballarino, Physica C 468 (2008) 2143–2148.
[17] M. Schwarz, K.P. Weiss, R. Heller, W.H. Fietz, Fusion Eng. Des. 84 (2009) 1748–1750.
[18] G.F. de la Fuente, J.C. Diez, L.A. Angurel, J.I. Pena, A. Sotelo, R. Navarro, Adv. Mater. 7 (1995) 853-856.
[19] M.F. Carrasco, R.A. Silva, N.J.O. Silva, R.F. Silva, J.M. Vieira, F.M. Costa, Appl. Surf. Sci. 255 (2009) 5503–5506.
[20] M.F. Carrasco, V.S. Amaral, R.F. Silva, J.M. Vieira, F.M. Costa, Appl. Surf. Sci. 252 (2006) 4957–4963.
[21] B. Ozkurt, M. A. Madre, A. Sotelo, M. E. Yakinci, B. Ozcelik, J. Supercond. Nov. Magn. 25 (2012) 799-804.
[22] A. Sotelo, Sh. Rasekh, M. A. Madre, J. C. Diez, J. Supercond. Nov. Magn. 24 (2011) 19-25.
[23] A. Sotelo, M. Mora, M.A. Madre, J.C. Diez, L.A. Angurel, G.F. de la Fuente, J. Eur. Ceram. Soc. 25 (2005) 2947-2950.
[24] A. Sotelo, M.A. Madre, J.C. Diez, Sh. Rasekh, L.A. Angurel, E. Martinez, Supercond. Sci. Technol. 22 (2009) 034012.
[25] V.V. Lennikov, P.E. Kazin, Y.D. Tretyakov, G.F. de la Fuente, Z. Anorg. Allg. Chem. 630 (2004) 2337-2342.

[26] M. Mora, L.A. Angurel, J.C. Diez, R.J. Drost, P.H. Kes, Physica C 372–376 (2002) 1179-1182.
[27] L.A. Angurel, G.F. de la Fuente, A. Badia, A. Larrea, J.C. Diez, J.I. Pena, E. Martinez, R. Navarro: A.V. Narlikar (Ed.), Studies of High Temperature Superconductors, vol. 21, Nova Science Publishers, New York, 1997, pp. 1-31.
[28] J. Jaroszynski, F. Hunte, L. Balicas, Youn-jung Jo, I. Raičević, A. Gurevich, D.C. Larbalestier, F.F. Balakirev, L. Fang, P. Cheng, Y. Jia, H.H. Wen, Phys. Rev. B 78 (2008) 174523.
[29] A. Sidorenko, V. Zdravkov, V. Ryazanov, S. Horn, S. Klimm, R. Tidecks, A. Wixforth, Th. Koch, Th. Schimmel, Phil. Mag. 85 (2005) 1783-1790.
[30] X.L. Wang, A.H. Li, S. Yu, S. Ooi, K. Hirata, C.T. Lin, E.W. Collings, M.D. Sumption, M. Bhatia, S.Y. Ding, S.X. Dou, J. Appl. Phys. 97 (2005) 10B114.
[31] T.T.M. Palstra, B. Batlogg, R.B. van Dover, L.F. Schneemeyer, J.V. Waszchak, Phys. Rev. B 41 (1990) 6621-6632.
[32] D. Sharma, R. Kumar, V.P.S. Awana, Solid State Commun. 152 (2012) 941–946.
[33] Y. Yeshurn, A.P. Malozemoff, Phys. Rev. Lett. 60 (1988) 2202-2205.
[34] N.Y. Fogel, V.G. Cherkasova, O.A. Koretzkaya, A.S. Sidorenko, Phys. Rev. B 55 (1997) 85-88.
[35] O. Brunner, L. Antognazza, J.M. Triskone, L. Mieville, O. Fischer, Phys. Rev. Lett. 67 (1991) 1354-1357.
[36] H.H. Wen, A.F.Th. Hoekstra, R. Griessen, S.L. Yan, L. Fang, M.S. Si, Phys. Rev. Lett. 79 (1997) 1559-1562.
[37] P.W. Anderson, Y.B. Kim, Rev. Mod. Phys. 36 (1964) 39-43.
[38] Y. Abulafia, A. Shaulov, Y. Wolfus, R. Prozorov, L. Burlachkov, Y. Yeshurun, D. Majer, E. Zeldov, H. Wuhl, V.B. Geshkenbein, V.M. Vinokur, Phys. Rev. Lett. 77 (1996) 1596-1599.
[39] T. Naito, H. Fujishiro, J. Fujikami, IEEE T. Appl. Supercon. 21, (2011) 2828-2831.
[40] S. Castellazzi, M.R. Cimberle, C. Ferdeghini, E. Giannini, G. Grasso, D. Marre, M. Putti, A.S. Siri, Physica C 273 (1997) 314-322.
[41] V. Plechacek, J. Hejtmanek, Physica C 282-287 (1997) 2577-2578.
[42] V. Ashokan, B.D. Indu, Thin Solid Films 518 (2010) e28-e30.
[43] M.A. Aksan, O. Kizilaslan, E.N. Aksan, M.E. Yakinci, Physica B 407 (2012) 2820-2824.
[44] T. Chakraborty, B. Gahtori, A. Soni, G.S. Okram, S.K. Agrawal, S.Y. Chen, Y.K. Kuo, M.A.H. Ahsan, A. Rao, Solid State Commun. 151 (2011) 1117–1121.
[45] A. Biju, U. Syamaprasad, A. Rao, J.G. Xu, K.M. Sivakumar, Y.K. Kuo, Physica C 466 (2007) 69-75.
[46] P.F. Herrmann, C. Albrecht, J. Bock, C. Cottevieille, S. Elschned, W. Herkert, M.O. Lafod, H. Lauvray, A. Leriche, W. Nick, E. Preisler, H. Salzburger, J.M. Tourre, T. Verhaege, IEEE T. Appl. Supercon. 3 (1993) 876-888.
[47] E. Natividad, M. Castro, R. Burriel, L.A. Angurel, J.C. Diez, R. Navarro, Supercond. Sci. Technol. 15 (2002) 1022-1029.
[48] M. Matsukawa, F. Tatezaki, K. Noto, H. Fujishiro, K. Michishita, Y. Kubo, Cryogenics 34 (1993) 685-688.
[49] S. Nakamae, J. Schwartz, IEEE T. Appl. Supercon. 7 (1997) 1699-1702.
[50] K. Khrishana, N.P. Ong, Q. Li, G.D. Gu, N. Koshizuka, Science 277 (1997) 83-85.
[51] M.C. Sekhar, S.V. Suryanarayana, Physica C 415 (2004) 209-219.
[52] L. Forro, J. Lukatela, B. Keszei, Solid State Commun. 73 (1990) 501-505.
[53] A.B. Kaiser, Phys. Rev. B 35 (1987) 4677-4681.
[54] M.A. Aksan, M.E. Yakinci, J. Alloy. Comp. 385 (2004) 33-43.

[55] N. Nagaosa, P.A. Lee, Phys. Rev. Lett. 64 (1990) 2450-2453.

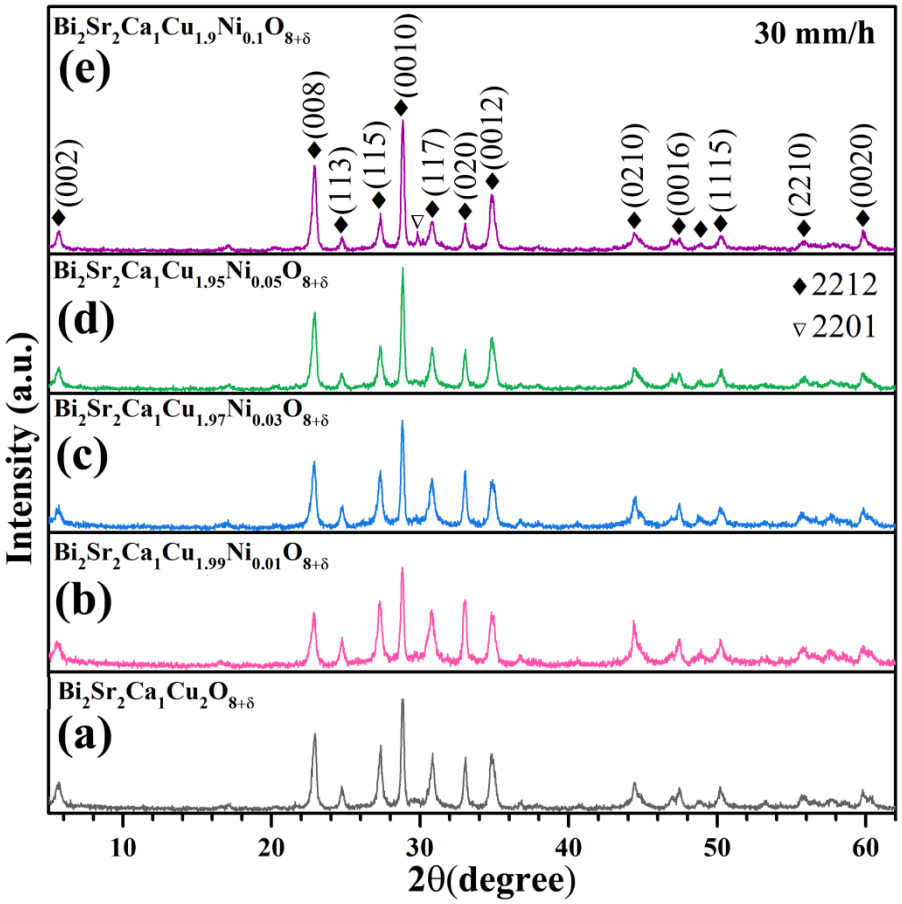

Figure 1. Powder XRD patterns of the G30 rods with stoichiometries $Bi_2Sr_2Ca_1Cu_{2-x}Ni_xO_{8+\delta}$ where **a)** x=0, **b)** x=0.01 **c)** x=0.03 **d)** x=0.05 **e)** x=0.1

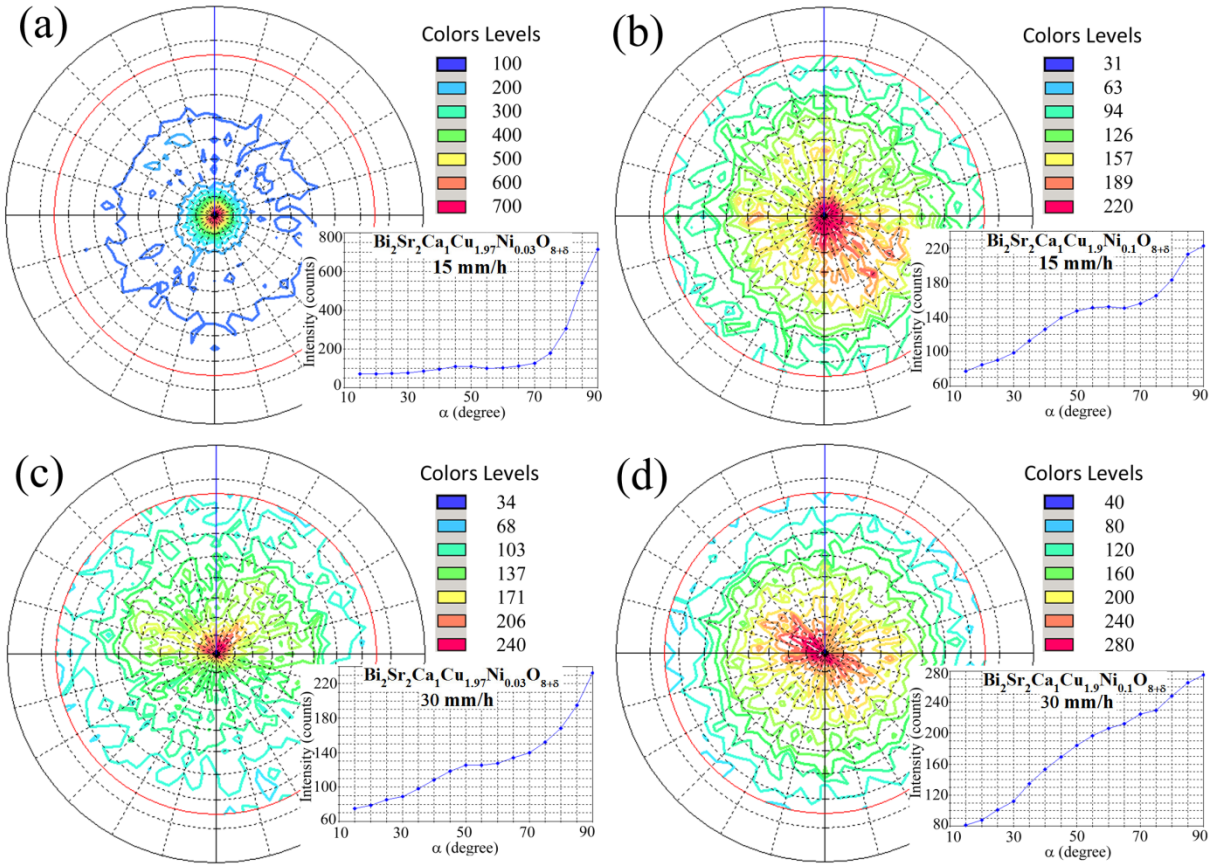

Figure 2. (020) pole figures and average intensities as a function of angle α are given together for some textured samples as representative examples. **a)** x=0.03, 15 mm/h **b)** x=0.1, 15 mm/h; **c)** x=0.03, 30 mm/h **d)** x=0.1, 30 mm/h.

Table I. Ratios, Intensity (α=90°)/Intensity (α=60°), obtained in the different rods used for quantification of alignment degree.

Composition	15 mm/h	30 mm/h
$Bi_2Sr_2CaCu_2O_{8+\delta}$	6.60	1.29
$Bi_2Sr_2CaCu_{1.99}Ni_{0.01}O_{8+\delta}$	6.64	1.46
$Bi_2Sr_2CaCu_{1.97}Ni_{0.03}O_{8+\delta}$	6.76	1.82
$Bi_2Sr_2CaCu_{1.95}Ni_{0.05}O_{8+\delta}$	2.83	1.53
$Bi_2Sr_2CaCu_{1.9}Ni_{0.1}O_{8+\delta}$	1.46	1.33

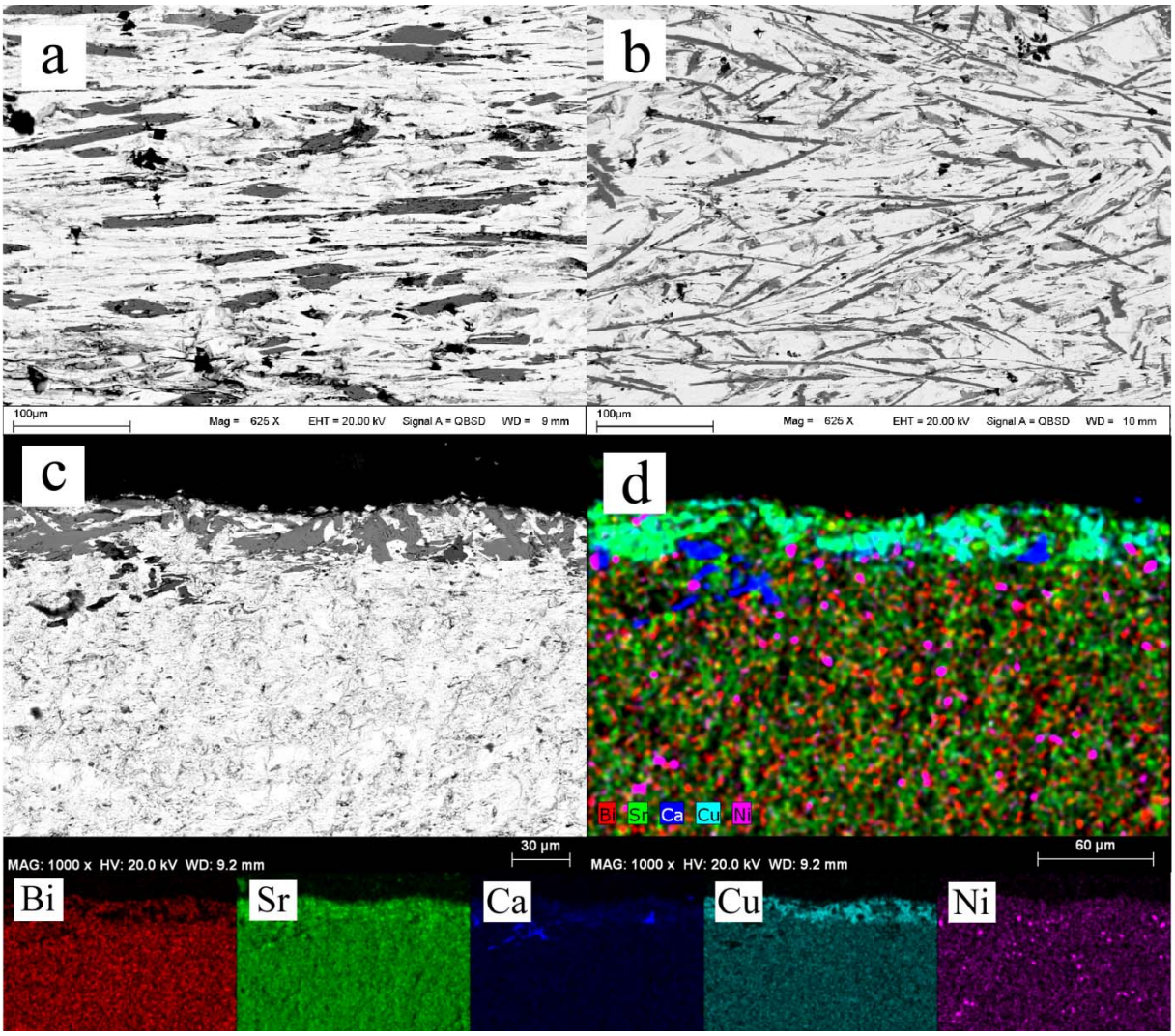

Figure 3. BSD images and elemental mapping analysis obtained on inner parts of longitudinal polished sections of both as-grown (a-b) and annealed rods (c-d) grown at 30 mm/h **(a)** x=0.01, **(b)** x=0.1, **(c,d)** x=0.1.

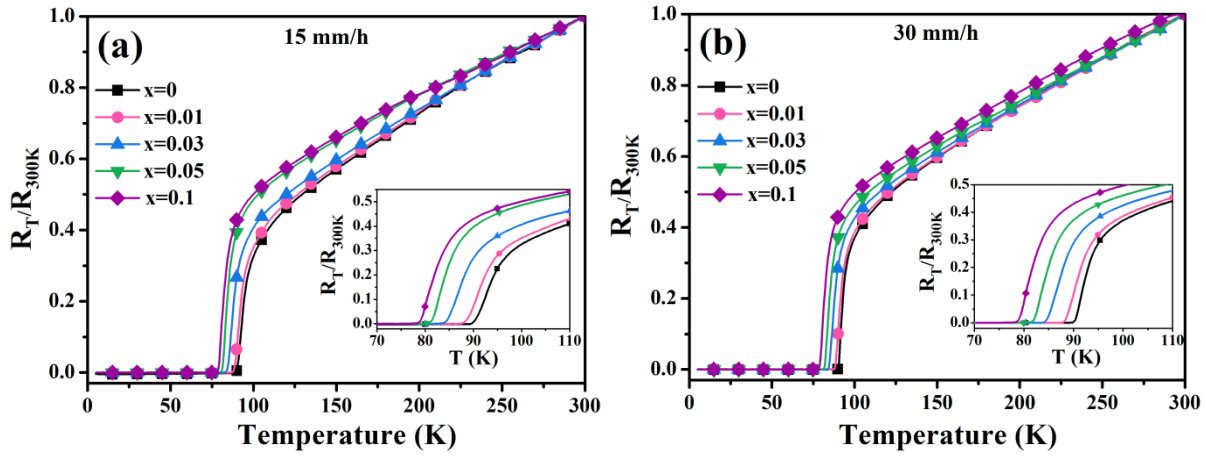

Figure 4. Temperature dependence of normalized resistivity of the **a)** G15, **b)** G30 rods substituted at different levels. Insets show the expanded view in the normal-to-superconducting transition region.

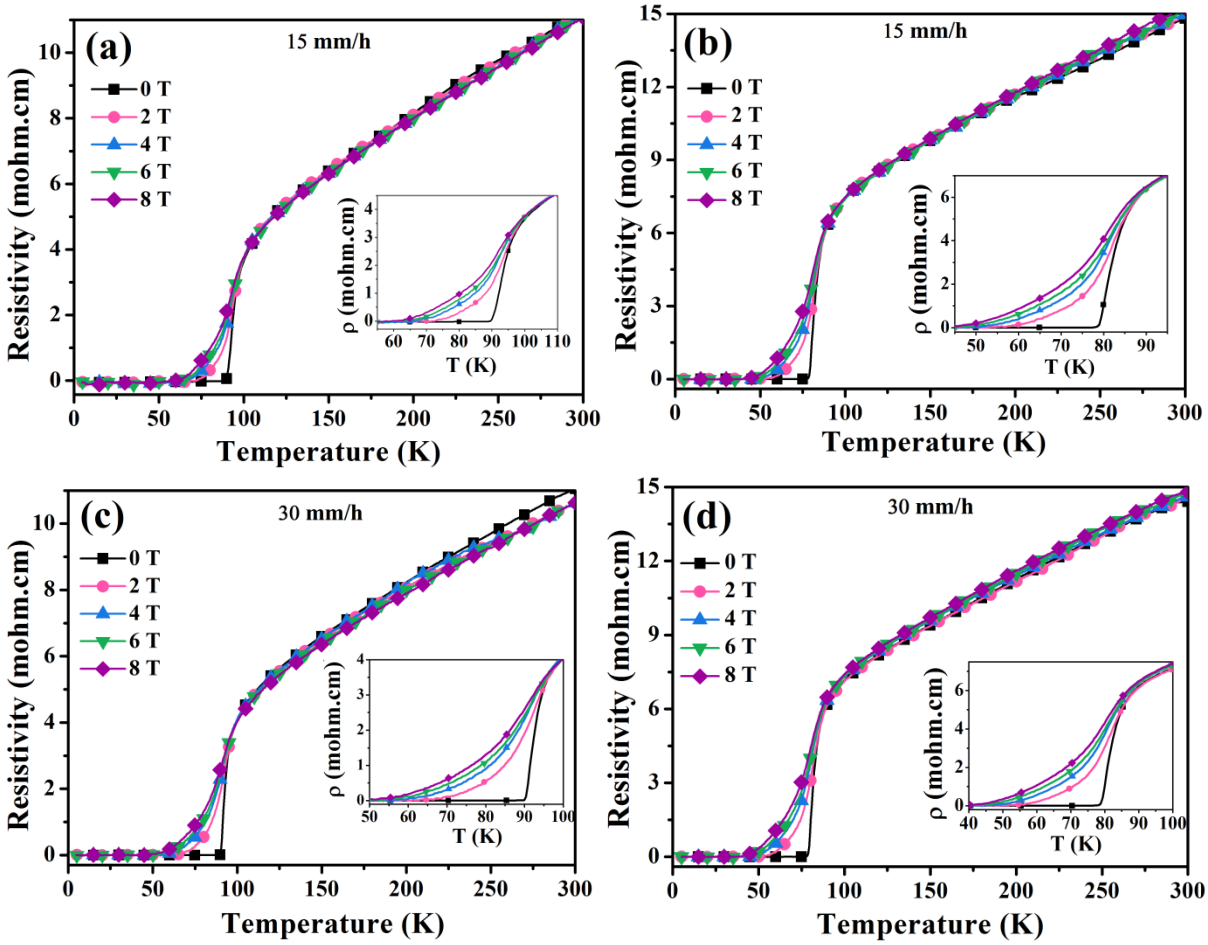

Figure 5. Representative *ρ-T* graphs of the rods at various magnetic fields in the range of 0–8 T. **a)** x=0, 15 mm/h **b)** x=0.1, 15 mm/h **c)** x=0, 30 mm/h **d)** x=0.1, 30 mm/h. Insets show the expanded view in the normal-to-superconducting transition region.

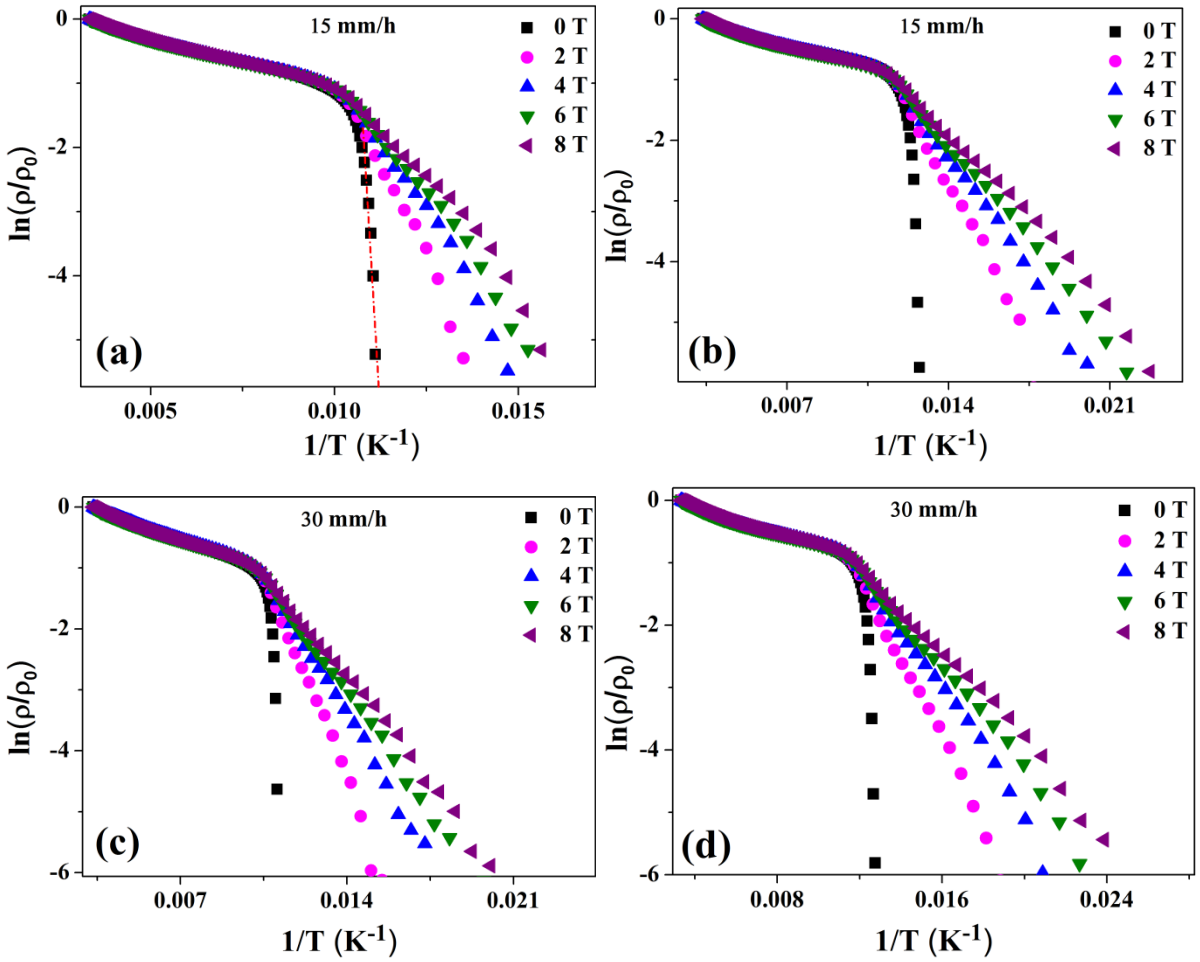

Figure 6. The Arrhenius plots of electrical resistance of the samples prepared at **a)** x=0, G15 **b)** x=0.1, G15 **c)** x=0, G30 and **d)** x=0.1, G30 for fields from 0 to 8 T. The dotted line in **(a)** represents the slope of the linear part of the low resistivity region used to calculate activation energy.

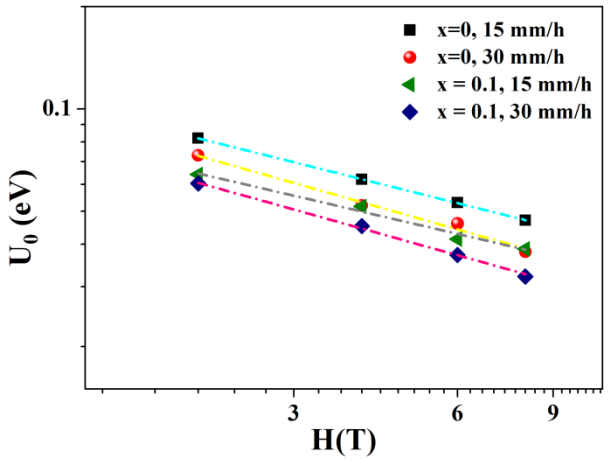

Figure 7. Field-dependent activation energy of the samples with different substitution and growth rates. The dotted lines indicate fitting curve of $U_0 \sim H^{-n}$.

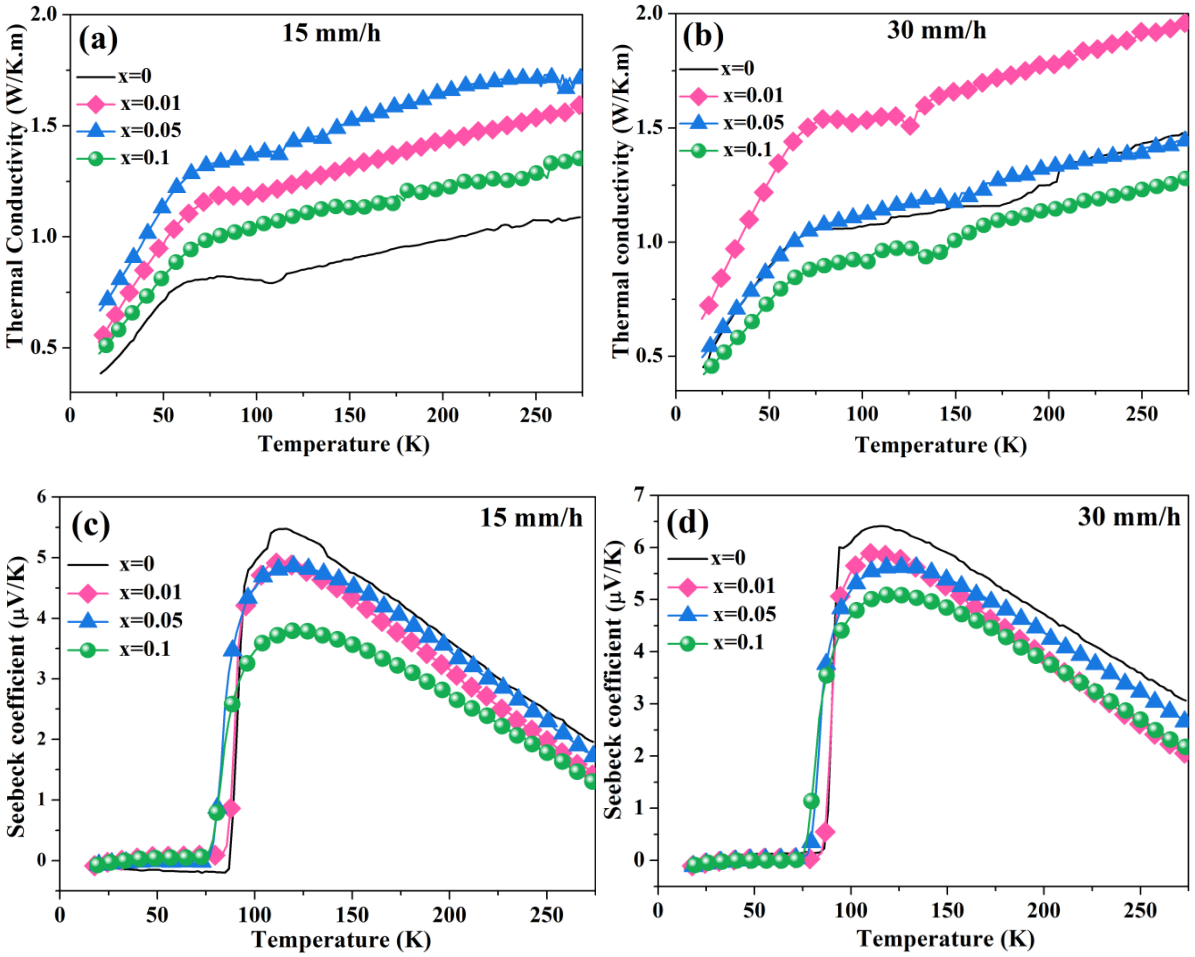

Figure 8. Temperature dependence of the **(a,b)** thermal conductivity,*κ*, **(c,d)** thermoelectric power,*S*, of the rods substituted at x=0, 0.01, 0.05 , 0.1 levels. The data in **(a,c)** and **(b,d)** belongs to G15 and G30 rods, respectively.